PAPER

Check for updates

Highly sensitive filterless near-infrared wavelength sensors with two self-driven MLG/Ge heterojunctions†

Yao-Zu Zhao,‡[a] Can Fu,‡[b] Feng-Xia Liang,*[a] Yu-Tian Xiao,[b] Jing-Yue Li,[b] Ming-Ming Liu,[a] Di Wu [ID][c] and Lin-Bao Luo [ID] *[b]

This paper reports a near-infrared wavelength sensor composed of two stacked monolayer graphene (MLG)/Ge heterojunction devices, which could enable the determination of the wavelength quantitatively. Since the absorption coefficient of Ge is wavelength dependent, the technical computer-aided design simulation shows a significant difference in the photon generation rate distribution of the two MLG/Ge photodetectors. Such a variation in photon absorption leads to a completely different evolution of the photocurrent in the stacked devices. Further experimental analysis found that the correlation between the photocurrent ratio (I_1/I_2) of the two MLG/Ge heterojunctions and the wavelength can be easily expressed using a monotonic function, by which the wavelengths in the near-infrared light range (880 nm to 1650 nm) could be calculated. It is worth noting that the detection band could be appropriately adjusted by changing the thickness of the Ge sheet employed in the photodetector. Moreover, the average relative error and average absolute error of the wavelength sensor are estimated to be 0.5% and 6.1 nm, respectively, which is comparable to the most investigated visible band wavelength sensor.

Introduction

Wavelength sensors that are able to identify wavelengths within a certain wavelength range play an important role in image sensing, visible light communications (VLCs), industrial inspection, spectroscopy, and biomedical sensing.[1–6] For instance, the color image sensor in the cell phone that separates different color signals through a color filter array is employed for VLCs.[7] In addition, humanoid eye-like sensor arrays made up of near-infrared organic photosensors and floating-gate memory modules possess distinguishing capability between visible light and infrared light, which can be further applied for nighttime monitoring and medical imaging.[8]

With the rapid development of optoelectronic devices, wavelength sensors with various device structures and operating mechanisms are designed to achieve color or accurate

wavelength detection.[1,2,7,9–11] So far, such sensors could be generally divided into two types, filter-assisted and filterless techniques. For example, one of the filter-assisted techniques, a grating spectrometer based on planar polymer waveguides made by deep reactive ion etching of the polymer, has been reported.[12] However, the major disadvantage of the filter-assisted photosensor is the need for additional filtering equipment (grating, optical filter, prisms, *etc.*), which correspondingly brings an extremely complex device structure and high production costs.[13] In addition, as an important complement to the filter-assisted wavelength sensors, filterless sensors have received increasing attention because they make the lower mass and smaller size possible.[14–17] The function of wavelength detection is mainly achieved by a vertical heterojunction, the usage of the narrowband material, or a gradient bandgap material for unfiltered wavelength sensors.[18–22] For example, Knipp D *et al.* developed an efficient wavelength sensor with the vertical arrangement of multiple perovskite diodes by changing the mixed halide perovskite components. The as-constructed wavelength sensor could be able to detect the spectrum from 400 to 700 nm, with a relatively lower color error of 3.6.[23] Nevertheless, the device is still limited to distinguish color and cannot quantitatively determine the wavelengths. Furthermore, Yang *et al.* reported an ultra-compact spectrometer made from a single compositionally engineered

a School of Materials Science and Engineering and Anhui Provincial Key Laboratory of Advanced Functional Materials and Devices, Hefei University of Technology, Hefei 230009, China. E-mail: fxliang@hfut.edu.cn

b School of Microelectronics, Hefei University of Technology, Hefei 230009, China

c School of Physics and Microelectronics, Zhengzhou University, Zhengzhou 450052, China. E-mail: luolb@hfut.edu.cn

† Electronic supplementary information (ESI) available: Fig. S1–S6. See DOI: https://doi.org/10.1039/d2tc01232d

‡ These authors contributed equally.

semiconductor nanowire, which could discriminate the wavelength of the incident irradiation quantitatively with a resolution of 15 nm in the visible range.[24] However, the harsh material preparation conditions and complicated device constructions are unfavorable for its further practical application. Lately, our group has developed several filterless wavelength sensors with two parallel devices, which could quantitatively determine the wavelengths ranging from 265 to 1050 nm through the relationship between the current ratio of the two devices and the wavelength.[25–27] Although the detector is optimized in terms of the device structure and function (good resolution in wavelength detection), its performance in the near-infrared range is still unsatisfactory. Inspired by this, we propose a new Ge-based wavelength sensor mainly concentrating on the near-infrared range.

In this work, we report a wavelength sensor consisting of two parallel monolayer graphene (MLG)/Ge heterojunction photodetectors (PDs). The technical computer-aided design (TCAD) simulation results present great changes in the photon generation rate of the double-heterojunction devices under the illumination of different wavelengths. Thus, the photocurrents displayed by the two heterojunctions are quite different from each other. Further photoelectric performance tests show that the wavelength sensor could easily detect wavelengths through the photocurrent ratio between the two PDs. The average relative error and average absolute error are calculated through a monotonic function, which are 0.5% and 6.1 nm, respectively, in the range from 880 nm to 1650 nm. It is noted that by fine-tuning the monotonic function, wavelengths at other light intensities could also be determined. We believe that this novel wavelength sensor has broad application prospects in future optoelectronic systems.

Results and discussion

Fig. 1a shows the schematic diagram of the as-fabricated wavelength sensor, which consists of two parallel MLG/Ge heterojunction PDs. The upper PD is named PD1 while the lower PD is named PD2. The detailed fabrication procedure of the MLG/Ge heterojunction PDs is provided in the Experimental section. Briefly, both the MLG/Ge heterojunction PDs are constructed by directly transferring chemical vapor deposition (CVD) grown graphene onto a photolithographically windowed n-type Ge wafer. Then, one PD with a similar device structure was placed above another. Fig. S1a (ESI†) displays the Raman spectrum of the graphene, which presents three main peaks, a weak D band, a strong G band, and a 2D band. Further careful examination found that the ratio of I_{2D}/I_G is 2.86, indicating that the as-synthesized graphene is the monolayer with neglectable defects.[28,29] The corresponding absorption spectrum of MLG is displayed in Fig. S1b, (ESI†), with only about 2–7% absorption of light in the range from ultraviolet to near-infrared.[30,31] This suggests that most incident light could pass through graphene and reach the Ge semiconductor below. In addition, the electrical properties of a single MLG/Ge
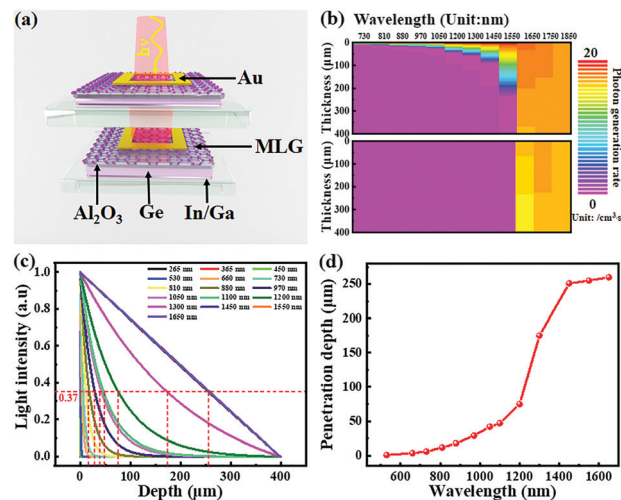

Fig. 1 (a) The geometry of a wavelength sensor composed of two vertically stacked MLG/Ge heterojunctions. (b) Simulated photon-generation rate under different wavelengths of illumination. (c) Light intensity attenuation curves. (d) The penetration depth of the incident light with different wavelengths.

heterojunction device were measured (Fig. S2a, ESI†), which showed a typical rectification behavior under dark conditions,[32] with a rectification ratio of about 27. Considering that Ag/graphene, Au/graphene, and Ge/In-Ga alloy are all ohmic contact (Fig. S2b, ESI†), the above rectification behavior can be exclusively attributed to the formation of a Schottky barrier between MLG and Ge. Through further measuring the current *versus* voltage (I–V) curves under light conditions, we found that the device also exhibits an obvious photovoltaic behavior, indicating that each single device could work without bias. Finally, the response speed of the as-fabricated single photodetector is evaluated, which presents a rise and fall times of (τ_r and τ_f) 32 and 20 μs, respectively (Fig. S3, ESI†).

The reason why such a stacked structure is designed lies in the fact that the different incident light displays the distinct optical absorption ability in the two devices. Fig. 1b presents the TCAD simulation results of the photon generation rate of the two stacked Ge materials (thickness: 400 μm/400 μm) under different lights (from 730 nm to 1850 nm). Note that the effect of MLG was neglected during the TCAD simulation, as it mainly acted as a transparent electrode here. From the results of Fig. 1b, we may draw the following conclusions: (1) the photon generation rate of each specific wavelength exhibits a decreasing trend in the depth direction. For example, when illuminated by the 730 nm incident light, the photon generation rate at the superficial surface of PD1 is as high as 4.67×10^{20}, while it decreases to 0 at the surface of PD2; (2) in the whole simulated wavelength range, the space with a relatively higher photon generation rate is extended, and gradually transferred from the surface of PD1 to the entire depth of PD2. For instance, PD2 begins to present an apparent photon generation rate from 1650 nm, which is about 2.17×10^{17} at its superficial surface. Without a doubt, the above simulation results are attributed to the decreasing absorption coefficient with

This journal is © The Royal Society of Chemistry 2022

J. Mater. Chem. C, 2022, **10**, 8474–8480 | **8475**

increasing wavelengths, as shown in Fig. S4 (ESI†). From the calculated absorption coefficient in Fig. S4, (ESI†) it is found that the absorption coefficient goes through a sharp decrease from about 10^6 to 10, with wavelength increasing from 300 nm to 1650 nm. Besides, the light intensity attenuation through the 400 μm Ge was simulated as well, which exhibited a similar tendency to the photon generation rate.[33] As presented in Fig. 1c and d, the intensity of each respective light decreases as it penetrates Ge, and the penetration depth (the physical depth that could absorb light) increases with the increasing wavelength. For instance, the penetration depth increases from about 1 μm to 260 μm, with the corresponding light tuning from 530 nm to 1650 nm. In brief, we could infer from the simulation results that the larger thickness (e.g., 400 μm) of PD1 is unfavorable for the penetration of the relatively shorter light (e.g., < 1650 nm), which may accordingly narrow the light detection range of the PD2 underneath. Therefore, in order to broaden the operating range of PD2 and the wavelength sensor, it is very necessary to fabricate PD1 with the appropriate thickness.

Next, a series of different device combinations employing the gradually decreased PD1 (thickness: from 389.9 μm to 53.2 μm) and the constant PD2 (thickness: 389.9 μm) are designed. Here, the ICP dry etching method was employed for Ge sheet thinning. Most notably, the thinnest thickness achieved in the experiment is about 53.2 μm and the Ge sheet will be damaged through continued etching. Fig. 2a presents a typical surface morphology of the etched germanium wafer, which shows a relatively smooth surface, with the etched surface fluctuating between ± 5 μm (Fig. 2b). Briefly, Fig. 3a draws the operation mechanism of the double-heterojunction devices. For each single MLG/Ge, there exist a depletion and diffusion region in the device.[34] Through further calculations, the width of the depletion region is about 3 μm, while the diffusion length (Lh) is about 700 μm for the n-type Ge (mobility: 1800 cm^{-2} Vs^{-1}) employed in our work (the detailed calculation procedure are given in the ESI†), and the total of which is much greater than the thickness of all the Ge used in each single PD. This result indicates that both the depletion and diffusion regions are within the whole depth of Ge wafer, and thus most of the absorbed light will contribute to the formation of the photocurrent. Fig. 3b plots the normalized photocurrent of the different PD device combinations measured at 0 V, where the
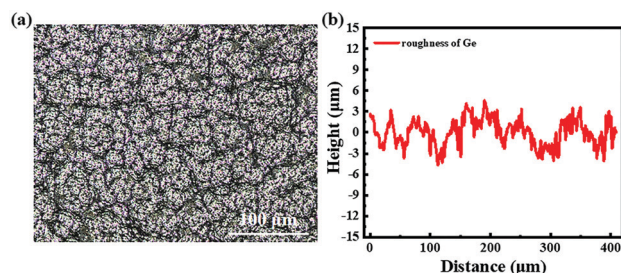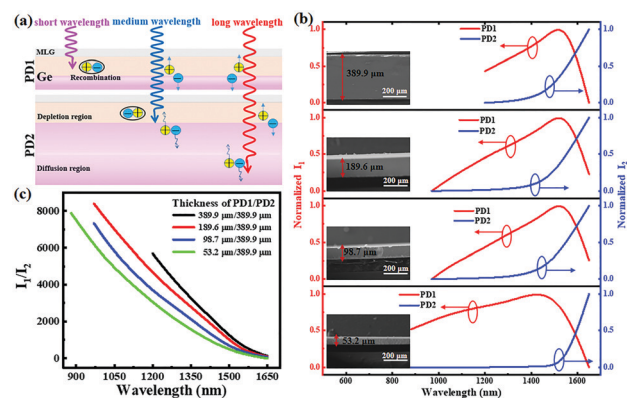

Fig. 3 (a) Schematic diagram of carrier generation for the wavelength sensor at different wavelengths. (b) Spectral responses of PD1 and PD2 with different thicknesses at a light intensity of 2 mW cm^{-2}, and the insets show the corresponding SEM images of Ge. (c) The photocurrent ratio as a function of wavelengths under different thicknesses.

inset displays the corresponding SEM images of PD1. Firstly, the two stacking PDs with a Ge thickness of 389.9/389.9 μm were measured and analyzed. Interestingly, as illuminated with the perpendicular incident light, the two PDs show completely different spectral selectivity. Obviously, PD1 shows a broadband optical response with a maximum response at 1550 nm, which is consistent with the reported bulk Ge material.[35] In contrast, PD2 exhibits a monotonic rising characteristic, which experiences a very slow increase first followed by a rapid increase. Note that PD2 presents an apparent photoresponse at a wavelength of 1200 nm and no photocurrent is observed for the wavelength shorter than 1200 nm. Moreover, the photocurrent of PD2 falls by several orders of magnitude compared with PD1 at 1200 nm. For example, the photocurrent of PD1 is as high as 1.46×10^{-3} mA, while its counterpart of PD2 remains only 2.57×10^{-7} mA. Then, the photocurrent of PD2 keeps increasing and reaches the same order of magnitude as PD1 at a wavelength of 1650 nm. All these spectral response characteristics in PD2 are reasonable, which is in accordance with the simulated results of the photon generation rate. Subsequently, the three-wavelength sensors with thinner Ge sheets (thickness: 189.6 μm, 98.7 μm, and 53.2 μm) for PD1 were prepared and tested sequentially. As expected, as the thickness of PD1 gradually decreased to 53.2 μm, the initial response wavelength of PD2 can be extended to the lower wavelength of 880 nm. Besides, the spectral responses of the respective PD1 and PD2 in these three device combinations have similar photoresponse features as that of the 389.9/389.9 μm wavelength sensor, except an apparent blue shift from 1550 nm to 1400 nm for PD1 with a thickness of 53.2 μm. Such a variation is explainable as the total adsorption of the longer light in 1550 nm may not compete for that in 1440 nm in such a thin thickness. To further condemn the above results, the simulated photocurrent of the devices under different conditions was also determined through TCAD. As shown in Fig. S5(a) (ESI†), the varying tendency of the photocurrent and spectral selectivity of both PDs are in good agreement with

Fig. 2 (a) The surface morphology and (b) surface roughness of germanium wafer after dry etching.

8476 | J. Mater. Chem. C, 2022, 10, 8474–8480

This journal is © The Royal Society of Chemistry 2022

the experiment results, except the very low photocurrent values for all the simulated results. For example, the simulated photocurrent of PD1 is about 8.9×10^{-3} μA for 1550 nm, which is three orders of magnitude smaller than the experimental results. On this account, the simulated photocurrent of PD2 exhibits no apparent photoresponse before 1500 nm. The reason for such a discrepancy in photocurrent values maybe attributed to the impact of the electrode contact, material interface and so on, during the complex photocurrent generation process. With regard to the Ge resistivity changing from 0.01 to 10 Ω cm (Fig. S5b, ESI†), the simulated photocurrent of the corresponding photodetectors exhibits a slight change, which will not affect the photocurrent ratio for the Ge (0.1–6 Ω·cm) employed in our work.

Although both PD1 and PD2 show quite different spectral responses in each device combination, it is surprising to find that the corresponding photocurrent ratio (I_1/I_2) as a function of the wavelength is monotonic for all wavelength sensors investigated (Fig. 3c), which is particularly important and provides the possibility for wavelength detection. Furthermore, the detection range could be successfully tuned through thickness, e.g., in the detection range of 880–1650 nm for 53.2/389.9 μm device, in comparison with its counterparts of 1200–1650 nm for the 389.9/389.9 μm device. Meanwhile, a slight decrease in the photocurrent ratio is observed as the thickness decreases, which is due to the less light adsorbed in the thinner material of PD1. From the above analysis, it can be concluded that the response range of the wavelength detector can be expanded to a certain extent by appropriately reducing the thickness of the first device, e.g., it could even reach the visible or UV region if the thickness of Ge could be tailored to several micrometres or nanometer level (see the penetration depth in Fig. S6, ESI†).

A further study shows that the relationship between the photocurrent ratio and wavelength is influenced by the light intensity. We measured the spectral response under a series of light intensity from 1.5 to 3.5 mW cm^{-2} for the stacked 53.2/389.9 μm device. Fig. 4a and b plots the light intensity-dependent photoresponse characteristics of PD1 and PD2 in the wavelength range of 880 nm to 1650 nm. Obviously, both I_1 and I_2 increase with the intensity of the light, which is understandable because stronger light produces more electron–hole pairs and thus higher photocurrents in the device. When I_1/I_2 is applied, the monotonic relationship is well preserved for all the measured light intensities, as displayed in Fig. 4c. Besides, the photocurrent ratio displays a negative correlation with the light intensity. Notably, a relatively high photocurrent ratio is observed at a low light intensity, which is consistent with the light intensity-dependent photocurrent ratio in a wider light intensity from 0.5 to 6.1 mW cm^{-2}, as shown in Fig. 4d. This finding is explainable, which may be originated from the lower penetration ability at a relatively lower light intensity. In such conditions, most photons are absorbed in the upper PD1, leading to a relatively higher I_1/I_2 at lower light levels.

While the investigated wavelength sensors under different thicknesses or light intensity indeed present a typical
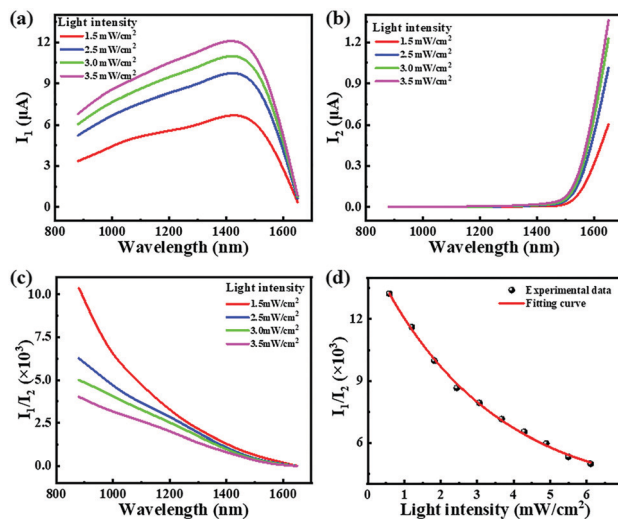

Fig. 4 Photocurrent of PD1 (a) and PD2 (b) under illumination of different intensities (1.5–3.5 mW cm^{-2}). (c) The relationship between the photocurrent ratio and the wavelength under light illumination with different intensities. (d) Photocurrent ratio as a function of the light intensity at a constant wavelength of 880 nm.

monotonic characteristic, how accurately it could describe the relationship between the photocurrent ratio and wavelength is still uncertain. In order to quantify the performance of the wavelength sensor, the stacked devices of 53.2/389.9 μm at a light intensity of 1.5 mW cm^{-2} were first picked for discussion in the following investigations. In fact, the high wavelength dependence of the photocurrent ratio could be quantitatively described by solving the strict monotonic function, which could be employed as the working curve of the wavelength sensor (Fig. 5a):
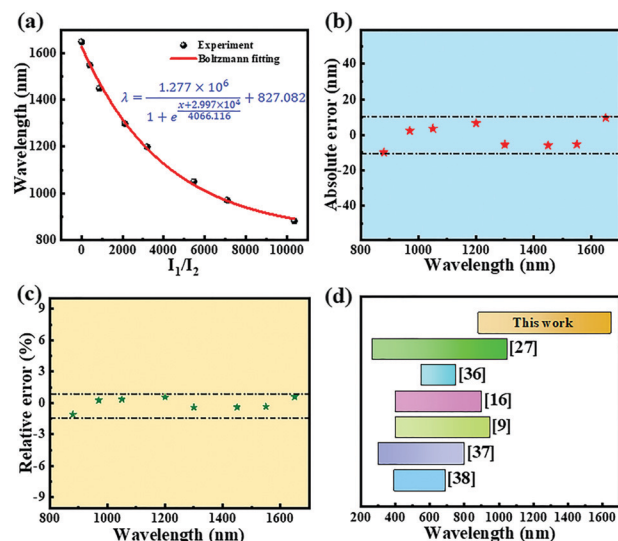

Fig. 5 (a) Fitting data: the red curve is the Boltzmann fitting. (b) The absolute error of the wavelength sensor. (c) The relative error of the wavelength sensor. (d) Comparison of the sensing range of the present sensor with other devices.

This journal is © The Royal Society of Chemistry 2022

J. Mater. Chem. C, 2022, **10**, 8474–8480 | **8477**

$$\lambda = \frac{1.277 \times 10^6}{1 + e^{\frac{x + 2.997 \times 10^4}{4066.116}}} + 827.082 \qquad (1)$$

where λ and x represent the wavelength and photocurrent ratio (I_1/I_2), respectively. Furthermore, the following equations 2 and 3 are provided to calculate the absolute and relative errors that reflect the degree of the deviation from the operating curve:

$$\text{Absolute error} = \lambda_e - \lambda_t \qquad (2)$$

$$\text{Relative error} = \frac{(\lambda_e - \lambda_t)}{\lambda_e} \times 100\% \qquad (3)$$

where λ_t and λ_e represent the theoretical and experimental photocurrent ratios, respectively. Fig. 5b and c summarize the absolute and relative errors of the wavelengths from 880 nm to 1650 nm. It can be observed that the average absolute error over the whole sensing range is 6.1 nm, while the maximum absolute error is 9.8 nm. In addition, the average relative error of the device is 0.5%, with a maximum relative error of 1.12% at 880 nm. The sensing errors of three specific wavelengths (880, 1050, and 1550 nm) at other different light intensities from 2.0 to 3.5 mW cm^{-2} were also calculated employing the above-mentioned method (Table 1), which are generally within the error range we described in Fig. 5b and c. All these demonstrate the high accuracy of the as-fabricated wavelength sensor in our work, which is comparable to the lately reported wavelength sensor in the visible range.[2,9,16,24,27] For a more complete description of the relationship between the photocurrent ratio and wavelength, a new fitting function is also achieved after taking into account the light intensity (see the ESI†). By using this function, the wavelength-dependent photocurrent ratio at various light intensities could be directly calculated. Finally, Fig. 5d gives a comparison of the operating range of the main wavelength sensor reported in the literature. Obviously, most of the current wavelength sensors are mainly used for UV light and visible light detection.[9,16,27,36–38] But our devices have a near-infrared sensing region from 880 nm to 1650 nm, which may have great potential in the optoelectronic devices and systems of the near-infrared sensing area.

Experimental section

Material synthesis and device manufacturing

In this work, a 389.9 μm thick antimony doped n-type (100) single crystal Ge wafer with a resistivity of 0.1–6 Ω cm (diameter: 4 inches, doping concentration of 10^{16} cm^{-3}, single-sided polishing) was purchased from Beijing Voskey Technology Co., Ltd. The Ge sheets of 189.6 μm, 98.7 μm, and 53.2 μm were obtained by ICP etching (working pressure: 3.6 Pa, gas flow $SF_6 : O_2 = 17 : 3$). In addition, high-quality single-layer graphene was grown by CVD at 1005 °C using a mixture of CH_4 (1 sccm) and H_2 (50 sccm), in which 50 μm thick copper foil was used as the catalytic substrate. The detailed growing process of graphene has been described in our previous work. After growth, the graphene film was spin-coated with 5 wt% polymethylmethacrylate (PMMA), and then, the underlying copper foil was removed in Marble reagent solution ($CuSO_4 :$ $HCl : H_2O = 10$ g $: 50$ mL $: 50$ mL). The graphene film was finally obtained through washing in deionized water to remove residual ions.

In order to assemble the MLG/Ge heterojunction device, the window pattern of the Ge wafer coated with about 50 nm thick alumina was defined by photolithography. Then, the treated Ge wafer was immersed in the dilute hydrochloric acid solution for about 8 hours, followed by soaking in deionized water. After this, Ge was slowly lifted to lay the graphene film onto its surface. Finally, the gold electrode was patterned by the shadow mask method through thermal evaporation technology. Silver paste and indium gallium alloy were coated on the top of the gold electrode and under the bottom of the Ge wafer, respectively. In order to assemble the wavelength sensor, we made a Ge-based device with the same structure, connected it to the top of another device, and blocked the light around it to prevent the light entering from the side.

Material characterization, device analysis, and simulation

Graphene films were studied by Raman spectroscopy (Horiba Jobin Yvon, LabRAM HR800). The absorption spectra of graphene in quartz and Ge were recorded using a Shimadzu UV-2550 UV-vis spectrophotometer. The morphology of Ge was characterized using a field-emission scanning electron microscope (FESEM, Gemini 500) and a 3D confocal laser microscope (VK-X250). The photoelectric characteristics were carried out using a semiconductor parameter test system (Keithley 2400). Before equipment analysis, the power intensity of the incident light was calibrated using a power meter (Thorlabs GmbH., PM 100D). All studies were performed at room temperature. Before the analysis with TCAD, the positions, angles of the light, and light intensity were finely defined to better simulate the optical properties of the device. Then, the spectra of the evolution of the photogeneration rate in different colors were drawn through the contours drawing component.

Table 1 Analysis of the error between the theoretical and the measured wavelengths

λ_{exp} (nm)	Light intensity (mW cm^{-2})	I_1/I_2	λ_{cal} (nm)	Absolute error (nm)	Relative error (nm)
880	1.5	10367.44	889.86	−9.86	−1.12
880	2.0	7886.32	887.13	−7.13	−0.81
880	2.5	6265.7	885.32	−5.32	−0.6
880	3.0	5002.8	885.38	−5.38	−0.61
880	3.5	4021.56	886.46	−4.46	−0.73
1050	1.5	5470.95	1046.37	3.63	0.35
1050	2.0	4866.0	1047.66	2.34	0.22
1050	2.5	4039.21	1055.82	−5.82	−0.55
1050	3.0	3622.54	1053.18	−3.18	−0.3
1050	3.5	2892.12	1046.89	3.11	0.29
1550	1.5	399.51	1555.25	−5.25	−0.34
1550	2.0	268.17	1543.35	6.65	0.43
1550	2.5	217.02	1546.5	3.5	0.23
1550	3.0	186.04	1556.18	−6.18	−0.4
1550	3.5	122.99	1552.63	−2.63	−0.17

8478 | *J. Mater. Chem. C*, 2022, **10**, 8474–8480

This journal is © The Royal Society of Chemistry 2022

Conclusions

In summary, we have successfully developed a wavelength sensor that consists of two identical MLG/Ge heterojunction PDs. According to TCAD simulations, the wavelength detection capability depends on the wavelength-dependent absorption coefficient. The relationship between the photocurrent ratio and wavelength follows a typical monotonic function by which the wavelength of the incident light can be determined. Further device analysis revealed that the detection range of the wavelength sensor varied from 1200–1650 nm to 880–1650 nm as the thickness of PD1 was decreased from 389.9 μm to 53.2 μm. For a 53.2 μm/389.9 μm device combination, it can quantitatively distinguish the wavelength of the incident light with an average relative error of 0.5% and an average absolute error of 6.1 nm at a light intensity of 1.5 mW cm^{-2}, which is comparable to other previously reported wavelength sensors. We believe that the present device configuration is also applicable to other semiconductor materials as long as there is a high dependence between the absorption coefficients and wavelengths, e.g., the narrow band gap materials of PbS and InGaAs have the potential for the near infrared wavelength sensor construction.

Author contributions

F. L. and L. L. conceived the experiments; Y. X. and J. L. performed the simulation; Y. Z. prepared the device fabrication and wrote the manuscript; C. F. analyzed the data from a theoretical perspective; D. W. and M. L. advised on device optimization. All the authors discussed the results and commented on the paper.

Conflicts of interest

The authors declare that they have no competing interests.

Acknowledgements

Notes and references

1 J. Cong, D. Yan, J. Tang, W. Guo and X. Mao, *IEEE Photonics Technol. Lett.*, 2019, **31**, 1979–1982.

2 J. H. Han, D. Kim, T.-W. Lee, Y. Jeon, H. S. Lee and K. C. Choi, *ACS Photonics*, 2018, **5**, 3322–3330.

3 R. F. Wolffenbuttel, G. d. Graaf and E. Engen, *Proceedings of ISCAS'95 – International Symposium on Circuits and Systems*, *IEEE* 1995, **1**, 299–302.

4 I. Dursun, C. Shen, M. R. Parida, J. Pan, S. P. Sarmah, D. Priante, N. Alyami, J. Liu, M. I. Saidaminov, M. S. Alias, A. L. Abdelhady, T. K. Ng, O. F. Mohammed, B. S. Ooi and O. M. Bakr, *ACS Photonics*, 2016, **3**, 1150–1156.

5 A. Căilean, B. Cagneau, L. Chassagne, M. Dimian and V. Popa, *IEEE Sens. J.*, 2015, **15**, 4632–4639.

6 N. Li, P. Mahalingavelar, J. H. Vella, D.-S. Leem, J. D. Azoulay and T. N. Ng, *Mater. Sci. Eng., R*, 2021, **146**, 100643.

7 K. Liang, C.-W. Chow and Y. Liu, *Opt. Express*, 2016, **24**, 9383–9388.

8 H. Wang, H. Liu, Q. Zhao, Z. Ni, Y. Zou, J. Yang, L. Wang, Y. Sun, Y. Guo, W. Hu and Y. Liu, *Adv. Mater.*, 2017, **29**, 1701772.

9 C. Richard, T. Courcier, P. Pittet, S. Martel, L. Ouellet, G.-N. Lu, V. Aimez and P. G. Charette, *Opt. Express*, 2012, **20**, 2053–2061.

10 N. Strobel, N. Droseros, W. Köntges, M. Seiberlich, M. Pietsch, S. Schlisske, F. Lindheimer, R. R. Schröder, U. Lemmer, M. Pfannmöller, N. Banerji and G. Hernandez-Sosa, *Adv. Mater.*, 2020, **32**, 1908258.

11 A. Reina, X. Jia, J. Ho, D. Nezich, H. Son, V. Bulovic, M. S. Dresselhaus and J. Kong, *Nano Lett.*, 2009, **9**, 30–35.

12 J. Mohr, B. Anderer and W. Ehrfeld, *Sens. Actuators, A*, 1991, **27**, 571–575.

13 R. Lukac and K. N. Plataniotis, *IEEE Trans. Broadcast Telev. Receivers*, 2005, **51**, 1260–1267.

14 A. Armin, R. D. Jansen-van Vuuren, N. Kopidakis, P. L. Burn and P. Meredith, *Nat. Commun.*, 2015, **6**, 6343.

15 Q. Lin, A. Armin, P. L. Burn and P. Meredith, *Nat. Photonics*, 2015, **9**, 687–694.

16 A. Polzer, W. Gaberl and H. Zimmermann, *Electron. Lett.*, 2011, **47**, 614–615.

17 Y. Li, C.-Y. Xu, J.-Y. Wang and L. Zhen, *Sci. Rep.*, 2014, **4**, 7186.

18 M. H. Paul, L. John and J. G. Rudolph, *Sensors and Camera Systems for Scientific, Industrial, and Digital Photography Applications V*, SPIE, 2004, vol. 5301, pp. 402–407.

19 W. Qarony, H. A. Khan, M. I. Hossain, M. Kozawa, A. Salleo, J. Y. Hardeberg, H. Fujiwara, Y. H. Tsang and D. Knipp, *ACS Appl. Mater. Interfaces*, 2022, **14**, 11645–11653.

20 J. A. Theil, M. Cao, G. Kooi, G. W. Ray, W. Greene, J. Lin, A. J. Budrys and U. Yoon, *MRS Online Proc. Libr.*, 2000, **609**, 143.

21 R. D. Jansen-van Vuuren, A. Armin, A. K. Pandey, P. L. Burn and P. Meredith, *Adv. Mater.*, 2016, **28**, 4766–4802.

22 M. Topic, H. Stiebig, D. Knipp and F. Smole, *IEEE Trans. Electron Devices*, 1999, **46**, 1839–1845.

23 M. I. Hossain, H. A. Khan, M. Kozawa, W. Qarony, A. Salleo, J. Y. Hardeberg, H. Fujiwara, Y. H. Tsang and D. Knipp, *ACS Appl. Mater. Interfaces*, 2020, **12**, 47831–47839.

24 Z. Yang, T. Albrow-Owen, H. Cui, J. Alexander-Webber, F. Gu, X. Wang, T.-C. Wu, M. Zhuge, C. Williams, P. Wang, V. Zayats Anatoly, W. Cai, L. Dai, S. Hofmann, M. Overend, L. Tong, Q. Yang, Z. Sun and T. Hasan, *Science*, 2019, **365**, 1017–1020.

25 L.-B. Luo, T. Fang, C. Xie, L. Wang, D. Wu and F.-X. Liang, *J. Mater. Chem. C*, 2021, **9**, 8855–8861.

This journal is © The Royal Society of Chemistry 2022

J. Mater. Chem. C, 2022, **10**, 8474–8480 | **8479**

26 F.-X. Liang, R.-Y. Fan, J.-Y. Li, C. Fu, J.-J. Jiang, T. Fang, D. Wu and L.-B. Luo, *Small*, 2021, **17**, 2102987.

27 C. Fu, Y.-T. Xiao, Y. Xing, X.-W. Tong, J. Wang, Z.-X. Zhang, L. Wang, D. Wu and L.-B. Luo, *ACS Appl. Mater. Interfaces*, 2021, **13**, 43273–43281.

28 S. Wang, B. D. Weil, Y. Li, K. X. Wang, E. Garnett, S. Fan and Y. Cui, *Nano Lett.*, 2013, **13**, 4393–4398.

29 G. H. Han, F. Güneş, J. J. Bae, E. S. Kim, S. J. Chae, H.-J. Shin, J.-Y. Choi, D. Pribat and Y. H. Lee, *Nano Lett.*, 2011, **11**, 4144–4148.

30 R. R. Nair, P. Blake, A. N. Grigorenko, K. S. Novoselov, T. J. Booth, T. Stauber, N. M.-R. Peres and A. K. Geim, *Science*, 2008, **320**, 1308.

31 C. Xie, P. Lv, B. Nie, J. Jie, X. Zhang, Z. Wang, P. Jiang, Z. Hu, L. Luo, Z. Zhu, L. Wang and C. Wu, *Appl. Phys. Lett.*, 2011, **99**, 133113.

32 L.-H. Zeng, M.-Z. Wang, H. Hu, B. Nie, Y.-Q. Yu, C.-Y. Wu, L. Wang, J.-G. Hu, C. Xie, F.-X. Liang and L.-B. Luo, *ACS Appl. Mater. Interfaces*, 2013, **5**, 9362–9366.

33 M. Arsalan, J. Liu, A. Zaslavsky, S. Cristoloveanu and J. Wan, *IEEE Trans. Electron Devices*, 2020, **67**, 3256–3262.

34 L. Wang, H. Luo, H. Zuo, J. Tao, Y. Yu, X. Yang, M. Wang, J. Hu, C. Xie, D. Wu and L. Luo, *IEEE Trans. Electron Devices*, 2020, **67**, 3211–3214.

35 L. Wang, J.-J. Li, Q. Fan, Z.-F. Huang, Y.-C. Lu, C. Xie, C.-Y. Wu and L.-B. Luo, *J. Mater. Chem. C*, 2019, **7**, 5019–5027.

36 Z. Wang, S. Yi, A. Chen, M. Zhou, T. S. Luk, A. James, J. Nogan, W. Ross, G. Joe, A. Shahsafi, K. X. Wang, M. A. Kats and Z. Yu, *Nat. Commun.*, 2019, **10**, 1020.

37 H. Sun, W. Tian, X. Wang, K. Deng, J. Xiong and L. Li, *Adv. Mater.*, 2020, **32**, 1908108.

38 J. Bao and M. G. Bawendi, *Nature*, 2015, **523**, 67–70.

8480 | *J. Mater. Chem. C*, 2022, **10**, 8474–8480

This journal is © The Royal Society of Chemistry 2022